J. Fluid Mech. (2018), *vol.* 857, *pp.* 784–805.
doi:10.1017/jfm.2018.762

Application of the minimum entropy production principle to shock reflection induced by separation

Chengpeng Wang[1,†], **Longsheng Xue**[1] **and Keming Cheng**[1]

[1]College of Aerospace Engineering, Nanjing University of Aeronautics and Astronautics, Nanjing, 210016, PR China

(Received 25 May 2018; revised 19 September 2018; accepted 20 September 2018; first published online 26 October 2018)

In this paper separation-induced shock reflection is studied theoretically and experimentally. An analytical model is proposed to establish the connections among upstream conditions, downstream conditions and shock configurations. Furthermore, the minimum entropy production principle is employed to determine the incident shock angles as well as the criterion for the transition from regular reflection to Mach reflection, which agrees well with experimental results. Additionally, a solution path for a reflected shock that fulfills the minimum entropy production principle is found in the overall regular reflection domain, based on which the steadiest shock configuration may be determined according to upstream and downstream conditions.

Key words: boundary layer separation, compressible flows, shock waves

1. Introduction

It is universally acknowledged that shock reflection is a fundamental phenomenon in supersonic flow, which exists widely in the internal and external flow fields of supersonic as well as hypersonic vehicles. Since Mach (1878) first studied two different shock reflection configurations, known as regular reflection (RR) and Mach reflection (MR), subsequent studies conducted by many researchers have never ceased. One of the hottest topics on reflection configurations is RR–MR transition, of which two classical criteria, the detachment criterion and the von Neumann criterion, were first proposed by von Neumann (1943, 1945). The reflected shock solution is related to flow deflection angle and pressure. Kawamura & Satto (1956) therefore introduced shock polar lines, i.e. pressure–deflection polar lines, to helpfully illustrate and analyse the shock configurations, based on which Ben-Dor (1991) summarized the reflection phenomena in steady, pseudo-steady and unsteady flows.

Most researches have mainly been focused on flow structures containing a single incident shock as well as double symmetrical incident shocks, while the flow field generated by asymmetrical geometry and multiple incident shocks may be more common in practical engineering applications. For a flow structure generated by double opposite asymmetrical ramps in steady flow (see Ivanov *et al.* 2002), the

† Email address for correspondence: wangcp@nuaa.edu.cn

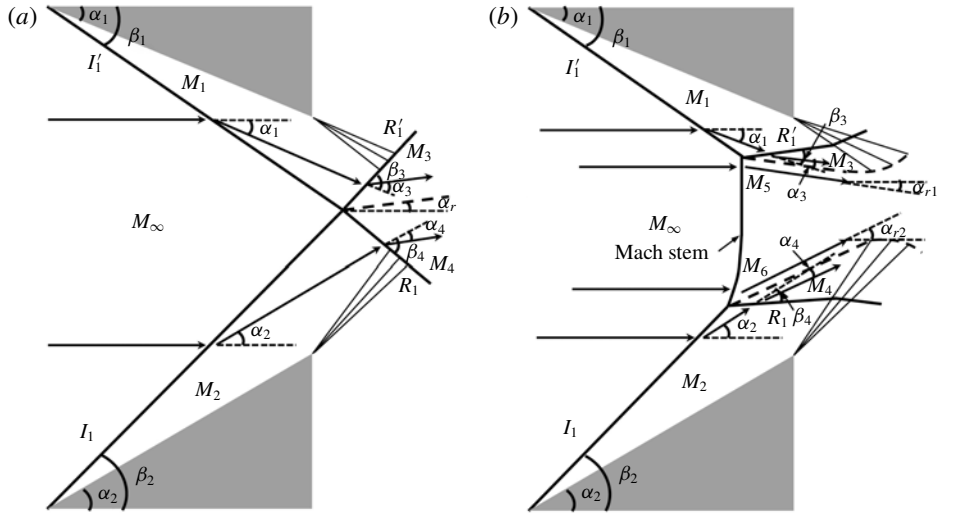

FIGURE 1. Schematic illustrations of possible shock reflections in steady flow: (*a*) overall RR, and (*b*) overall MR.

possible shock reflections are schematically illustrated in figure 1. The overall RR configuration, as shown in figure 1(*a*), consists of double asymmetrical incident shocks, denoted by I_1' on the top ramp and I_1 on the bottom ramp, respectively, and double asymmetrical reflected shocks, denoted by R_1' and R_1, respectively. An overall RR boundary condition requires that all the incident and reflected shocks meet at a single node, and the accompanying flow defection angles across the shocks must fulfill the equation

$$|\alpha_1 - \alpha_3| = |\alpha_2 - \alpha_4| = \alpha_r. \tag{1.1}$$

The overall MR, as shown in figure 1(*b*), is more complicated than the overall RR, of which a very strong curve shock, named Mach stem, is added to the configuration (see Azevedo & Liu 1993; Tao *et al.* 2017). Accordingly, incident shocks and reflected shocks cannot meet at a single node, which will be replaced by two endpoints of the Mach stem. The boundary condition of an overall MR hence becomes

$$\left.\begin{aligned} |\alpha_1 - \alpha_3| &= \alpha_{r1}, \\ |\alpha_2 - \alpha_4| &= \alpha_{r2}. \end{aligned}\right\} \tag{1.2}$$

The solutions of asymmetrical shock reflection can be indicated by pressure–deflection polar lines, which are illustrated in figure 2. There, I_1' and I_1 are the incident shock polar lines on the top and bottom ramps, respectively, along which the pressure fulfills the oblique shock wave equations (see Ben-Dor 1991; Li, Chpoun & Ben-Dor 1999). The solution of the reflected shock can be observed clearly by the intersection (denoted by point *a*) of reflected shock polar lines, i.e. R_1' and R_1. Assuming that I_1' remains stable, i.e. the reflected shock polar line of I_1' resides in R_1', while the ramp angle of I_1 ranges from a small enough degree to a big enough degree, then the admissible reflected shock polar lines of I_1 can be represented by R_1–R_5. Here R_2 and R_4 are two such typical lines: I_1' (or I_1, depending on α_1), R_1' and R_2 meet at a single point *b*; R_1' and R_4 are tangent at a single point *d*. According to the study conducted by Li *et al.* (1999), *b* and *d* are the two criteria of overall

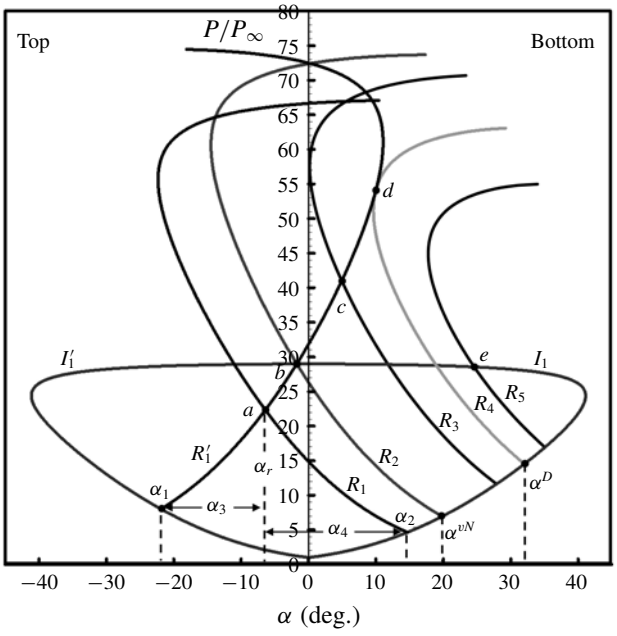

FIGURE 2. Pressure–deflection polar lines illustrating various possible solutions of asymmetric shock reflection in steady flows.

RR to overall MR transition, of which the ramp angles α^{vN} and α^D correspond to the von Neumann condition and the detachment condition, respectively. Accordingly, an overall RR solution resides in the domain where $\alpha_2 < \alpha^{vN}$, such as R_1; an overall MR solution resides in the domain where $\alpha_2 > \alpha^D$, such as R_5; while more than one analytic solution may reside in the domain where $\alpha^{vN} < \alpha_2 < \alpha^D$, such as R_3, which is known as the dual-solution domain (see Hu *et al.* 2009).

The RR–MR transition has been noticed for decades since some earlier research conducted by Hornung, Oertel & Sandeman (1979) and Hornung & Robinson (1982). However, it is still difficult to predict the reflected solution in the dual-solution domain, in which both the RR and MR configurations are stable. The second law of thermodynamics requires that a non-equilibrium state process will be in the direction of increasing entropy. As a supplement, the *a posteriori* axiom postulated by Glansdorff & Prigogine (1971) points out that the process must fulfill the principle of minimum entropy production, based on which Li & Ben-Dor (1996*a*,*b*) proposed new criteria of RR–MR transition in steady as well as unsteady flow, which agreed well with the experimental results obtained by Chpoun *et al.* (1995). Most of the theoretical models for reflection configuration analysis considered the upstream flow condition and geometric configuration, while the downstream flow condition should not be discarded in some practical engineering applications, which widely exists in supersonic as well as hypersonic inlets, isolators and combustion chambers (see Matsuo, Miyazato & Kim 1999). For an undisturbed flow, as shown in figure 3(*a*), the shock reflection structure is distinct and steady (see Wang, Xue & Tian 2017). However, due to the downstream flow disturbance, as shown in figure 3(*b*), shock–boundary layer interaction is usually typically characterized by local separation as well as massive separation (see Tao, Fan & Zhao 2014; Wang

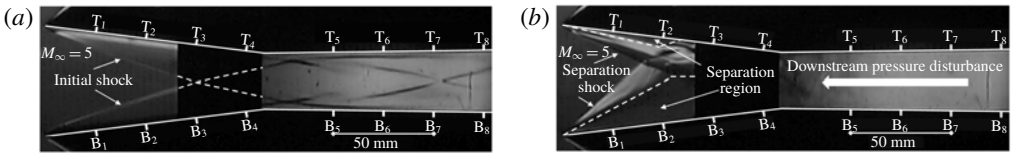

FIGURE 3. Schlieren images illustrating RR configurations at $M_\infty = 5$: (*a*) induced by ramps, and (*b*) induced by separations.

et al. 2015; Xue, Wang & Cheng 2018). Similar to the geometric configuration, the separation region, the leading edge of which can be regarded as a virtual wedge, also induces a separation shock, accompanied by shock reflection, including RR and MR configurations, which was proved by Tao *et al.* (2014). Differently, however, it is hard to predict the leading-edge angle of the separation region due to the uncertain shape determined by the downstream disturbance, which leads to a relatively steady or unsteady shock structure in a steady upstream flow.

Therefore, the connection among upstream flow, downstream flow and shock structure should be established. Aiming to solve this problem, an analytical method is proposed here based on previous contributions. In this method, an equivalent back-pressure $\overline{\overline{p}}$ is defined to measure the influence of downstream flow disturbance. Furthermore, the principle of minimum entropy production is employed to predict the separation shock angle as well as the criterion of RR–MR transition. Finally, a solution path of the reflected shock that indicates the steadiest reflection configuration is found in the overall RR domain, which agrees well with experimental results.

2. Analytical methods in current study

2.1. *Equivalent back-pressure* $\overline{\overline{p}}$

The initial shocks in steady flow, which are induced by symmetrical ramps, generate symmetrical regular reflections, as shown in figure 3(*a*). Previous studies of this model conducted by Wang *et al.* (2017) found that the effect of downstream pressure was characterized by the upstream motion of the shock train, accompanied by asymmetric flow structures. When the downstream influence is intensified strongly enough, separation regions appear on the top and bottom ramps and induce asymmetric regular reflection, as shown in figure 3(*b*). Compared with the initial shock reflection without the downstream effect, the separation-induced reflection is more complicated, with the shock angles of the leading edge on the top and bottom enlarging to different degrees, and the flow structures can be relatively steady or unsteady.

The flow structures around ramps in figure 3 are simplified to sketches as depicted in figure 4. The reflections induced by ramps (figure 3*a*) are easy to analyse via pressure–deflection polar lines, which is shown in figure 5(*a*). Under the upstream conditions of free-stream Mach number of 5 and two symmetrical ramps of 7°, the polar lines obviously demonstrate that the reflection solution of point *a* is much lower than von Neumann criterion of point *b*; the structure is therefore a symmetrical overall regular reflection. However, in separation flow, the reflection solution cannot be obtained by ramp angles directly. It has been proved that the massive separation can be considered as a virtual wedge for the flow field (see Chapman, Kuehn & Larson 1958; Délery & Marvin 1986; Wang *et al.* 2015). Accordingly, the separation regions on ramps, the flow pattern of which is schematically depicted in figure 4(*b*),

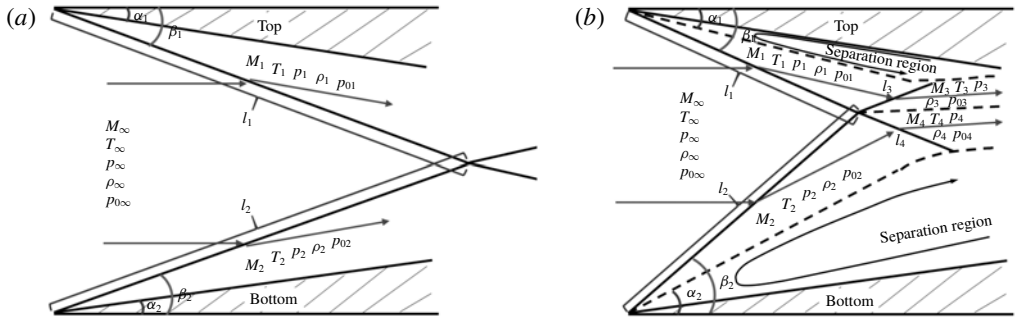

FIGURE 4. Sketches of overall RR configurations: (*a*) induced by ramps, and (*b*) induced by separations.

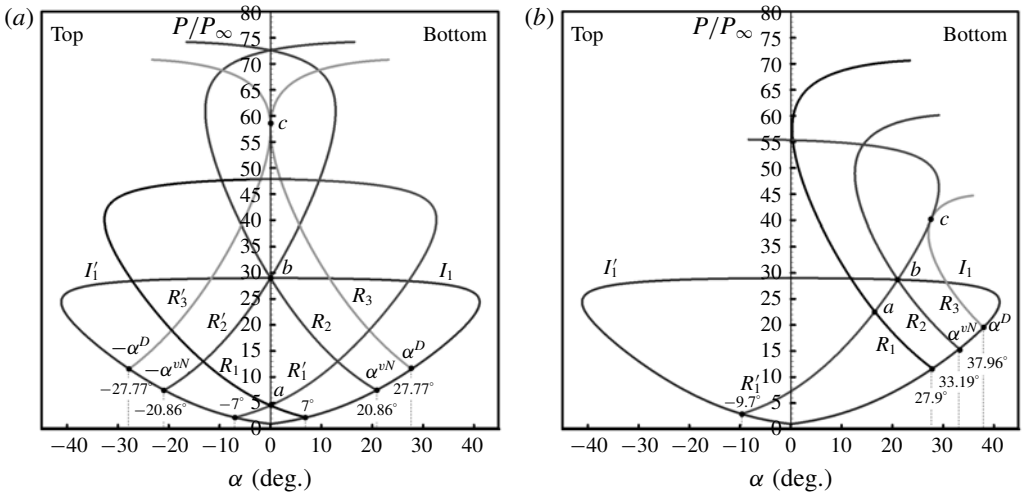

FIGURE 5. Pressure–deflection polar lines at $M_\infty = 5$: (*a*) symmetrical reflection induced by ramp, and (*b*) asymmetrical reflection induced by separation.

are regarded as new ramps with enlarged angles (α_1, α_2). Then the shock polar theory can be employed to analyse the separation-induced shock reflection, and the accompanying pressure–deflection polar line is depicted in figure 5(*b*). Herein the asymmetric reflection solution of point *a* is also within the von Neumann criterion of point *b*; however, it is hard to say that the shock configuration could always be a regular reflection under a steady upstream flow condition. The most distinct difference between ramp-induced reflection and separation-induced reflection is that the former is mainly determined by the upstream flow condition while the latter depends on the downstream flow condition. This means that the solution point *a* can be anywhere, including the overall RR solution, overall MR solution or dual-solution domains at different compression wedge angles, which will be analysed in the following sections. Furthermore, different from the upstream flow, the downstream flow is not uniform; hence it is difficult to the describe downstream flow condition with common physical parameters. Therefore, it is necessary to introduce a novel measurement for the downstream flow condition before discussing the results.

To measure the effect of downstream flow disturbance, an equivalent back-pressure, represented by $\overline{\overline{p}}$, is proposed in the present study. As shown in figure 6(*a*), *L* (solid

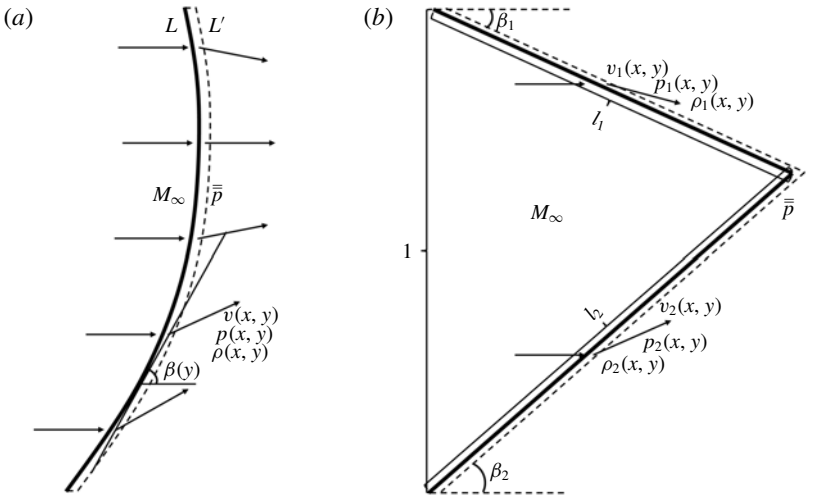

FIGURE 6. Schematic illustrations of shock wave: (*a*) a curved shock, and (*b*) a simplified incident shock for current study.

line) is assumed as a two-dimensional curved shock wave with uniform upstream flow and non-uniform downstream flow. The upstream flow is in the x direction, and the parameters v, p and ρ are assumed as constants ahead of L, while they are related to (x, y) coordinates after L. Also, L' (dashed line) is assumed as a curved line, which is very close to L. The parameters, which can be determined by M_∞ and local shock angle $\beta(y)$ via oblique shock wave equations, are limited in the local region between L and L'. Then, $\bar{\bar{p}}$ is defined as follows:

$$\left.\begin{aligned} \bar{\bar{p}} &= \frac{\int \rho v p \,\mathrm{d}L}{\int \rho v \,\mathrm{d}L}, \\ \rho &= f_\rho(M_\infty, \beta), \\ p &= f_p(M_\infty, \beta), \\ v &= f_v(M_\infty, \beta). \end{aligned}\right\} \tag{2.1}$$

Back-pressure $\bar{\bar{p}}$ is defined to measure the background integral pressure level that the downstream pressure disturbance exerts in the local region close to the leading shock wave. The equations above demonstrate that $\bar{\bar{p}}$ is determined by the upstream Mach number, the local shock angle and the local mass flow rate. For the current study, the leading shock wave of the separation-induced flow structure is simplified as in figure 6(*b*), and hence (2.1) becomes

$$\bar{\bar{p}} = \frac{\int \rho_1 v_1 p_1 \,\mathrm{d}l_1 + \int \rho_2 v_2 p_2 \,\mathrm{d}l_2}{\int \rho_1 v_1 \,\mathrm{d}l_1 + \int \rho_2 v_2 \,\mathrm{d}l_2}. \tag{2.2}$$

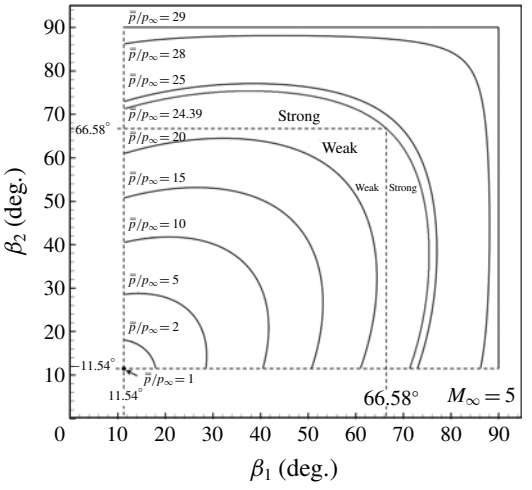

FIGURE 7. Diagram illustrating the relation among β_1, β_2 and $\bar{\bar{p}}$.

2.2. *Relation between regular reflection and* $\bar{\bar{p}}$

For the separation-induced reflection, the current study focuses on the local flow field ahead of and behind the shock wave, and hence the heat exchange of the fluid may be neglected in the analysis. Therefore, equation (2.2) can be simplified to

$$\bar{\bar{p}} = \frac{p_1\rho_1 M_1\sqrt{T_1}k_1 + p_2\rho_2 M_2\sqrt{T_2}k_2}{\rho_\infty M_\infty\sqrt{T_\infty}}. \tag{2.3}$$

Herein, the coefficients k_1 and k_2 are

$$\left.\begin{aligned} k_1 &= \frac{\cos\beta_2\sin(\beta_1-\alpha_1)}{\sin(\beta_1+\beta_2)}, \\ k_2 &= \frac{\cos\beta_1\sin(\beta_2-\alpha_2)}{\sin(\beta_1+\beta_2)}, \end{aligned}\right\} \tag{2.4}$$

where β_1 and β_2 are the shock angles on the top and bottom ramps, respectively, and α_1 and α_2, which are treated as virtual wedge angles, can be obtained by

$$\left.\begin{aligned} \alpha_1 &= \arctan\left(\frac{M_\infty^2\sin^2\beta_1 - 1}{[1 + M_\infty^2(\frac{1}{2}(\gamma+1) - \sin^2\beta_1)]\tan\beta_1}\right), \\ \alpha_2 &= \arctan\left(\frac{M_\infty^2\sin^2\beta_2 - 1}{[1 + M_\infty^2(\frac{1}{2}(\gamma+1) - \sin^2\beta_2)]\tan\beta_2}\right). \end{aligned}\right\} \tag{2.5}$$

Equations (2.3)–(2.5) indicate that all the parameters are related to the upstream Mach number and shock angles, hence any one of β_1, β_2 and $\bar{\bar{p}}$ can be obtained from the other two. The relation diagram among β_1, β_2 and $\bar{\bar{p}}$ is illustrated in figure 7. It is confirmed that the solutions of β_1 and β_2 are in a same curve under the condition of the same $\bar{\bar{p}}$. Therefore, the solutions tend to be stable where there needs to be a criterion, which will be analysed in the following.

2.3. *Relation between entropy production and $\bar{\bar{p}}$ in regular reflection*

The minimum entropy production principle is employed for the current study. According to Li & Ben-Dor (1996*a*,*b*), for a simplified shock wave passing through a uniform supersonic flow, as shown in figure 6(*a*), the entropy production $\dot{S}$ can be obtained as

$$\dot{S} = \int_L \rho v \Delta s \, \mathrm{d}y, \tag{2.6}$$

where Δs is the entropy change across the shock wave L. Since the total entropy production due to successive shocks would be negligible compared with that of a normal shock (see Crocco 1958; Matsuo *et al.* 1999), only the entropy production generated by incident and reflected shock waves is considered in an RR flow field. The total entropy production of the shock configuration shown in figure 4(*b*) can be written as

$$\dot{S} = \int_{l_1} \rho_1 v_1 \Delta s_1 \, \mathrm{d}y + \int_{l_2} \rho_2 v_2 \Delta s_2 \, \mathrm{d}y + \int_{l_3} \rho_3 v_3 \Delta s_3 \, \mathrm{d}y + \int_{l_4} \rho_4 v_4 \Delta s_4 \, \mathrm{d}y. \tag{2.7}$$

The flows, which are limited to local regions ahead of and behind shocks, can be assumed as uniform, and the parameters are determined by the incident and reflected shocks. Then (2.7) can be reduced to

$$\dot{S} = \rho_1 v_1 \Delta s_1 k_1 l + \rho_2 v_2 \Delta s_2 k_2 l + \rho_3 v_3 \Delta s_3 k_3 l + \rho_4 v_4 \Delta s_4 k_4 l, \tag{2.8}$$

where l is the entrance height, k_1 and k_2 have been given by (2.4), and k_3 and k_4 are

$$\left.\begin{aligned} k_3 &= k_1 \sin(\beta_3 - \alpha_r), \\ k_4 &= k_2 \sin(\beta_4 - \alpha_r), \end{aligned}\right\} \tag{2.9}$$

where α_r is the solution of the RR, i.e. the flow deflection angle across the incident and reflected shocks, and β_3 and β_4 are the reflected shock angles of the incident shocks on the top and bottom, respectively. Since heat exchange has been neglected, i.e. the total temperature is constant, the entropy change across one shock wave can be written via the total pressure as

$$\Delta s = -C_v(\gamma - 1) \ln\left(\frac{p_{02}}{p_{01}}\right), \tag{2.10}$$

where p_{01} and p_{02} are the total pressures ahead of and behind the shock, respectively. For computational convenience, $\ddot{S}$ is defined as follows:

$$\ddot{S} = \frac{\dot{S}}{C_v(\gamma - 1)\rho_\infty M_\infty l \sqrt{\gamma R T_\infty}}. \tag{2.11}$$

The upstream flow is assumed to be a uniform and steady flow; hence the definition of $\ddot{S}$ is a factor of $\dot{S}$, which can reflect the total entropy production absolutely. Inserting (2.8) and (2.10) into (2.11) results in

$$\begin{aligned} \ddot{S}_{RR} = & -\frac{\rho_1}{\rho_\infty}\frac{M_1}{M_\infty}\sqrt{\frac{T_1}{T_\infty}} \ln\left(\frac{p_{01}}{p_{0\infty}}\right) k_1 - \frac{\rho_2}{\rho_\infty}\frac{M_2}{M_\infty}\sqrt{\frac{T_2}{T_\infty}} \ln\left(\frac{p_{02}}{p_{0\infty}}\right) k_2 \\ & - \frac{\rho_3}{\rho_1}\frac{\rho_1}{\rho_\infty}\frac{M_3}{M_1}\frac{M_1}{M_\infty}\sqrt{\frac{T_3}{T_1}}\sqrt{\frac{T_1}{T_\infty}} \ln\left(\frac{p_{03}}{p_{01}}\right) k_3 \\ & - \frac{\rho_4}{\rho_2}\frac{\rho_2}{\rho_\infty}\frac{M_4}{M_2}\frac{M_2}{M_\infty}\sqrt{\frac{T_4}{T_2}}\sqrt{\frac{T_2}{T_\infty}} \ln\left(\frac{p_{04}}{p_{02}}\right) k_4, \end{aligned} \tag{2.12}$$

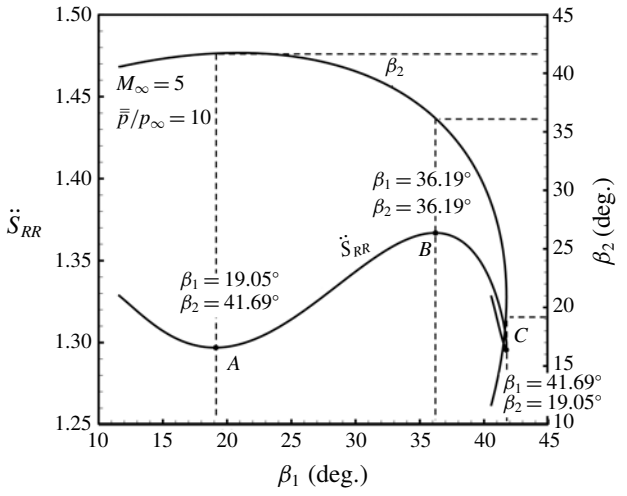

FIGURE 8. Diagram illustrating the relation among β_1, β_2 and $\ddot{S}_{RR}$.

where the coefficients k_1, k_2, k_3 and k_4 have been given by (2.4) and (2.9), respectively. Equation (2.12) indicates that all the fractions can be obtained by all the incident and reflected shock angles and the Mach numbers ahead of the shocks. Since the reflected shocks are determined by the incident shocks, and the upstream parameters are constant, $\ddot{S}$ is related only to the incident shock angles, i.e. β_1 and β_2. It has been proved above that any one of β_1, β_2 and $\bar{\bar{p}}$ can be obtained from the other two; hence $\ddot{S}_{RR}$ can be written as

$$\ddot{S}_{RR} = f_{SRR}(M_\infty, \beta_1, \bar{\bar{p}}), \tag{2.13}$$

where M_∞ is the upstream flow condition, $\bar{\bar{p}}$ is the downstream flow condition, and β_1 represents the shock configuration. The connection between total entropy production and the regular reflection induced by separation is therefore established.

2.4. *Application of the minimum entropy production principle to regular reflection*

Equation (2.13) indicates that $\ddot{S}_{RR}$ can be obtained from M_∞, β_1 and $\bar{\bar{p}}$, and the relation diagram is illustrated in figure 8 under the upstream and downstream conditions of $M_\infty = 5$ and $\bar{\bar{p}}/p_\infty = 10$, respectively. There, points A and C fulfill the conditions that

$$\left.\begin{aligned} \frac{\partial f_{S_{RR}}}{\partial \beta_1} &= 0, \\ \frac{\partial^2 f_{S_{RR}}}{\partial^2 \beta_1} &\geqslant 0. \end{aligned}\right\} \tag{2.14}$$

This results in $\beta_1 = 19.05°$, $\beta_2 = 41.69°$, or $\beta_1 = 41.69°$, $\beta_2 = 19.05°$, which correspond to two asymmetrical RR configurations that fulfill the minimum entropy production. In figure 8 point B fulfills the conditions that

$$\left.\begin{aligned} \frac{\partial f_{S_{RR}}}{\partial \beta_1} &= 0, \\ \frac{\partial^2 f_{S_{RR}}}{\partial^2 \beta_1} &\leqslant 0. \end{aligned}\right\} \tag{2.15}$$

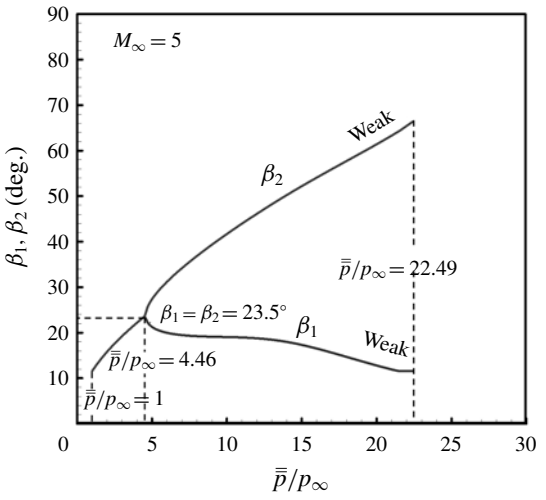

FIGURE 9. Diagram illustrating the relation between $\bar{\bar{p}}$ and incident shock angles that fulfill the minimum entropy production.

This results in $\beta_1 = \beta_2 = 36.19°$, which corresponds to a symmetrical RR that fulfills the local maximum entropy production. It is obvious that the entropy production of asymmetrical RR is much less than that of a symmetrical RR at the conditions of $M_\infty = 5$ and $\bar{\bar{p}}/p_\infty = 10$. For further work, the solutions under the conditions of (2.14) with a steady $M_\infty = 5$ and an increasing $\bar{\bar{p}}$ are calculated and illustrated in figure 9. There, $1 < \bar{\bar{p}}/p_\infty \leqslant 22.49$ are the boundary conditions for the existence of solutions. The diagrams demonstrate that a symmetrical shock configuration will fulfill the minimum entropy production at a small downstream condition ($\bar{\bar{p}}/p_\infty \leqslant 4.46$). Furthermore, there is no solution when $\bar{\bar{p}}/p_\infty > 22.49$ due to the reflected shocks approaching the detachment condition, and the shock configuration will be replaced by Mach reflection, which will be analysed below.

2.5. *Relation between Mach reflection and* $\bar{\bar{p}}$

A flow field of separation-induced MR is depicted schematically in figure 10. Since a Mach stem takes part in the shock configuration which contributes to the total mass flow rate, the function of $\bar{\bar{p}}$ should become

$$\bar{\bar{p}} = \frac{\int \rho_1 v_1 p_1 \,\mathrm{d}l_1 + \int \rho_2 v_2 p_2 \,\mathrm{d}l_2 + \int \rho_5 v_5 p_5 \,\mathrm{d}l_0}{\int \rho_1 v_1 \,\mathrm{d}l_1 + \int \rho_2 v_2 \,\mathrm{d}l_2 + \int \rho_5 v_5 \,\mathrm{d}l_0}, \tag{2.16}$$

where l_0 is the ratio of Mach stem length to entrance height. The Mach stem is a strongly curved shock (see Gao & Wu 2010; Bai & Wu 2017; Tao *et al.* 2017), the pressure change of which is close to that of a normal shock, hence it may be treated as a section of a normal shock in the current study. Then (2.16) can be written as

$$\bar{\bar{p}} = \frac{1}{\rho_\infty M_\infty \sqrt{T_\infty}} (p_1 \rho_1 M_1 \sqrt{T_1} k_1' + p_2 \rho_2 M_2 \sqrt{T_2} k_2' + p_5 \rho_5 M_5 \sqrt{T_5} l_0), \tag{2.17}$$

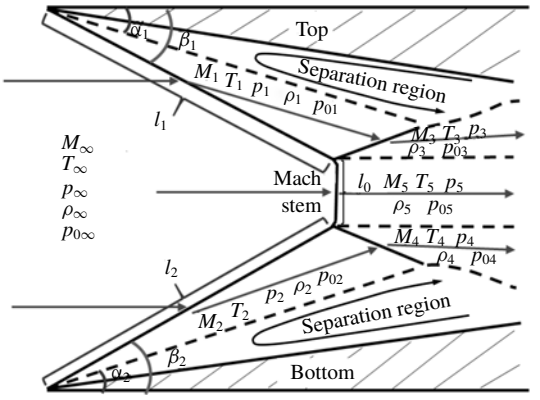

FIGURE 10. Sketch of overall MR induced by separation.

where the coefficients k_1' and k_2' are obtained by

$$\left.\begin{aligned} k_1' &= \frac{\cos\beta_2 \sin(\beta_1-\alpha_1)(1-l_0)}{\sin(\beta_1+\beta_2)}, \\ k_2' &= \frac{\cos\beta_1 \sin(\beta_2-\alpha_2)(1-l_0)}{\sin(\beta_1+\beta_2)}. \end{aligned}\right\} \tag{2.18}$$

2.6. *Relation between entropy production and* $\overline{\overline{p}}$ *in Mach reflection*

Equations (2.16)–(2.18) indicate that there is an additional variable l_0 in the function of $\overline{\overline{p}}$. Hence the factor $\ddot{S}$ of total entropy production should add to the contribution of l_0 and results in

$$\begin{aligned} \ddot{S}_{MR} = &-\frac{\rho_1}{\rho_\infty}\frac{M_1}{M_\infty}\sqrt{\frac{T_1}{T_\infty}}\ln\left(\frac{p_{01}}{p_{0\infty}}\right)k_1' - \frac{\rho_2}{\rho_\infty}\frac{M_2}{M_\infty}\sqrt{\frac{T_2}{T_\infty}}\ln\left(\frac{p_{02}}{p_{0\infty}}\right)k_2' \\ &-\frac{\rho_3}{\rho_1}\frac{\rho_1}{\rho_\infty}\frac{M_3}{M_1}\frac{M_1}{M_\infty}\sqrt{\frac{T_3}{T_1}}\sqrt{\frac{T_1}{T_\infty}}\ln\left(\frac{p_{03}}{p_{01}}\right)k_3' \\ &-\frac{\rho_4}{\rho_2}\frac{\rho_2}{\rho_\infty}\frac{M_4}{M_2}\frac{M_2}{M_\infty}\sqrt{\frac{T_4}{T_2}}\sqrt{\frac{T_2}{T_\infty}}\ln\left(\frac{p_{04}}{p_{02}}\right)k_4' \\ &-\frac{\rho_5}{\rho_\infty}\frac{M_5}{M_\infty}\sqrt{\frac{T_5}{T_\infty}}\ln\left(\frac{p_{05}}{p_{0\infty}}\right)l_0, \end{aligned} \tag{2.19}$$

where k_1' and k_2' have been given by (2.18), and k_3' and k_4' are

$$\left.\begin{aligned} k_3' &= k_1'\sin(\beta_3-\alpha_{r1}), \\ k_4' &= k_2'\sin(\beta_4-\alpha_{r2}). \end{aligned}\right\} \tag{2.20}$$

Here α_{r1} and α_{r2} are the solutions of MR, i.e. the flow deflection angles across incident and reflected shocks on the top and bottom, respectively; and β_3 and β_4 are the reflected shock angles of incident shocks on the top and bottom, respectively. Because $\overline{\overline{p}}$ cannot be obtained from β_1 and β_2, $\ddot{S}_{MR}$ is related to four variables and can be written as

$$\ddot{S}_{MR} = f_{SRR}(M_\infty, \beta_1, \beta_2, \overline{\overline{p}}). \tag{2.21}$$

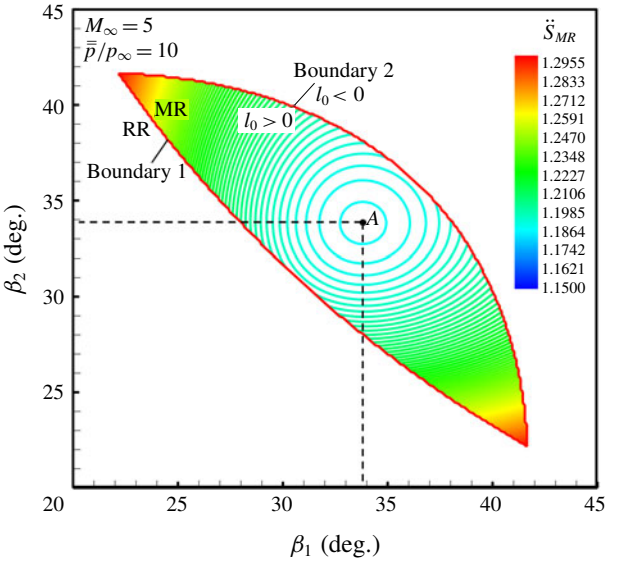

FIGURE 11. (Colour online) Contour lines of entropy production factor illustrating the relation among β_1, β_2 and $\ddot{S}_{MR}$.

2.7. *Application of the minimum entropy production principle to Mach reflection*

According to (2.21), figure 11 illustrates the relation contour lines among β_1, β_2 and $\ddot{S}_{MR}$ under the upstream and downstream conditions of $M_\infty = 5$ and $\bar{\bar{p}} = 10$, respectively. The boundary 1 is the lower limit that fulfills the von Neumann criterion, i.e. the existence of MR solution; boundary 2 is the upper limit that keeps $0 < l_0 < 1$, which means that it is impossible that the length of the Mach stem will be negative or longer than the height of the entrance. The possible solutions of MR reside in the region between boundary 1 and boundary 2. Point A fulfills the conditions that

$$\left.\begin{aligned} \frac{\partial^2 f_{MR}}{\partial\beta_1\partial\beta_2} &= 0, \\ \frac{\partial^2 f_{MR}}{\partial^2\beta_1} &\geqslant 0, \\ \frac{\partial^2 f_{MR}}{\partial^2\beta_2} &\geqslant 0. \end{aligned}\right\} \tag{2.22}$$

This results in $\beta_1 = \beta_2 = 33.82°$, which corresponds to a structure that fulfills the minimum entropy production. Hence the total entropy production of a symmetrical MR induced by separation is less than that of asymmetrical ones, which is different from that of RR under the same conditions. For further work, the solutions that fulfill the conditions of (2.22) with a steady $M_\infty = 5$ and an increasing $\bar{\bar{p}}$ are calculated and illustrated in figure 12. There, $\bar{\bar{p}}/p_\infty = 7.58$ and $\bar{\bar{p}}/p_\infty = 29$ are the minimum and maximum downstream conditions for the existence of Mach reflection, respectively. As can be seen, the structure under different values of $\bar{\bar{p}}/p_\infty$ that fulfills the minimum entropy production always keeps the shock angles at $\beta_1 = \beta_2 = 33.82°$, and it is only characterized by an increasing Mach stem.

Since the solutions that fulfill the minimum entropy production both exist in RR and MR, there needs to be a comprehensive analysis.

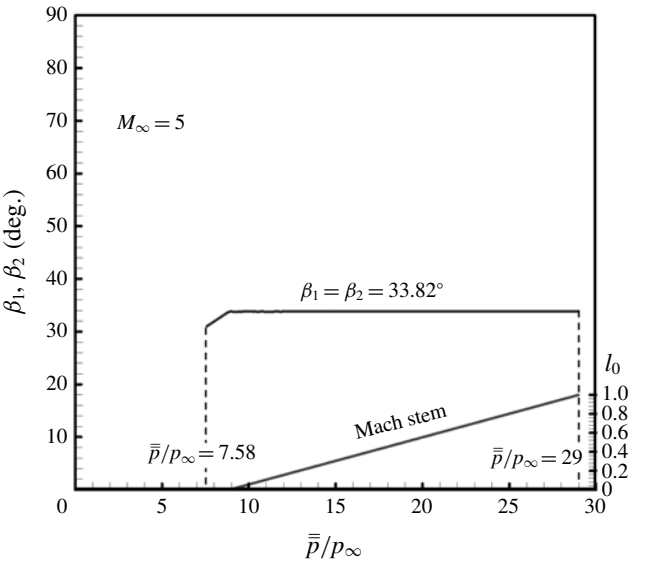

FIGURE 12. Diagram illustrating the relation between $\bar{\bar{p}}$ and incident shock angles as well as Mach stem that fulfill the minimum entropy production.

2.8. *Comprehensive analysis in RR and MR induced by separation*

The methods mentioned above establish the connection among upstream flow, shock configurations and downstream flow in separation-induced RR and MR, respectively. To compare the characteristics of minimum entropy production between RR and MR, the entropy production factors as well as flow deflection angles that fulfill the minimum entropy production are calculated and illustrated together in figure 13. There, $\ddot{S}_{RR}$ and $\ddot{S}_{MR}$ are the minimum entropy production factors of RR and MR, respectively; α_{RR1} and α_{RR2} are the flow deflection angles of RR on the top and bottom, respectively; α_{MR} is the flow deflection angle of MR on the top or bottom (they are a same angle); and α^{vN} and α^{D} are the von Neumann condition and detachment condition, respectively. As indicated in figure 13, seven typical positions are marked from (i) to (vii) and explained as follows:

(i) $\bar{\bar{p}}/p_\infty = 1$ is the minimum downstream condition for the existence of shock reflection solutions;

(ii) $\bar{\bar{p}}/p_\infty = 4.46$ is the minimum downstream condition for the existence of asymmetrical RR solutions;

(iii) $\bar{\bar{p}}/p_\infty = 7.58$ is the minimum downstream condition for the existence of MR solutions;

(iv) $\bar{\bar{p}}/p_\infty = 13.05$ is a critical downstream condition for the possibility of RR–MR transition;

(v) $\bar{\bar{p}}/p_\infty = 18.39$ is another critical downstream condition for the possibility of RR–MR transition;

(vi) $\bar{\bar{p}}/p_\infty = 22.49$ is the maximum downstream condition for the existence of RR solutions;

(vii) $\bar{\bar{p}}/p_\infty = 29$ is the maximum downstream condition for the existence of MR solutions.

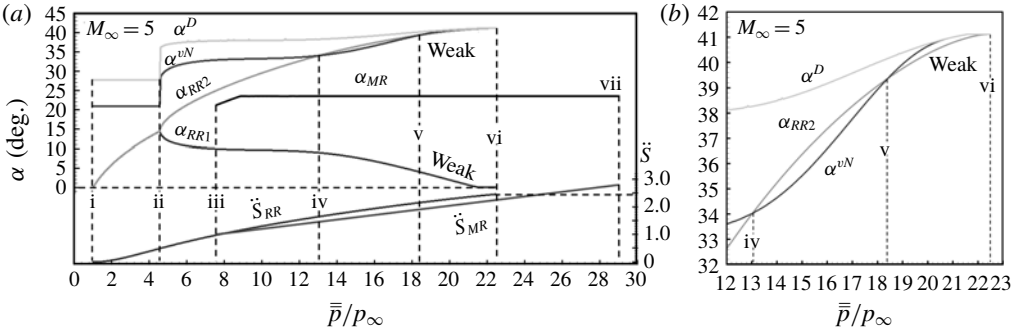

FIGURE 13. Diagrams illustrating the relations between $\bar{\bar{p}}$ and entropy production factors as well as flow deflection angles in RR and MR that fulfill the minimum entropy production: (*a*) whole diagram, and (*b*) detailed diagram for $12 \leqslant \bar{\bar{p}}/p_\infty \leqslant 23$.

It can be seen from the typical positions that the entropy production factor of MR is lower than that of RR during the overlapping stage, i.e. $\ddot{S}_{MR} < \ddot{S}_{RR}$ when $7.58 < \bar{\bar{p}}/p_\infty < 22.49$. However, RR cannot transfer to MR until α_{RR2} reaches the von Neumann condition, i.e. $\alpha_{RR2} \geqslant \alpha^{vN}$ when $13.05 \leqslant \bar{\bar{p}}/p_\infty \leqslant 18.39$ (figure 13*b*), which means $\bar{\bar{p}}/p_\infty = 13.05$ is a criterion of downstream condition for RR–MR transition. It is more complicated during $18.39 \leqslant \bar{\bar{p}}/p_\infty \leqslant 22.49$, as shown in figure 13(*b*). There, the solutions that fulfill the minimum entropy production can reside in overall RR as well as overall MR, depending on the former structure: if the former structure reaches von Neumann condition, then the current structure will be MR; if not, it will be RR, which means the structure is unsteady during this condition stage.

Base on the comprehensive analysis above, the relation between $\bar{\bar{p}}$ and shock reflection configurations induced by separation is illustrated in figure 14. There, RR_S and RR_{AS} denote symmetrical and asymmetrical RR, respectively; MR_S is symmetrical MR; β_1 and β_2 are the incident shock angles of RR induced by separation on the top and bottom, respectively (β_1 and β_2 are interchangeable); β_0 is the shock angle of MR induced by separation (the angles on the top and bottom are the same); and l_0 is the ratio of the Mach stem length to the entrance height. The critical solution of RR–MR transition is $\beta_1 = 19°$, $\beta_2 = 48°$ (or $\beta_1 = 48°$, $\beta_2 = 19°$), which will be verified by experimental results in the following sections.

3. Experimental results and discussions

3.1. *Experimental apparatus and test model*

The experiment was conducted in a hypersonic wind tunnel; previous research in this facility has been described in detail by Wang *et al.* (2017). There are some improved parts in the current test, as shown in figure 15. Firstly, a plug device driven by a stepper motor, which can generate a linearly increasing throttling (see Xue *et al.* 2018), was employed to guide the downstream pressure disturbance. Secondly, 16 Kulite XTEL-190M fast-response transducers, which were operated at a rate of 10 kHz using data acquisition cards and a 10 s sampling time, were mounted along the central lines of ramps on the top and bottom, respectively. Lastly, a NAC (NAC Image Technology) Hotshot High Speed Camera, which operated at a frame rate of 5 kHz with a 6 s sampling time and a resolution of 608 × 436 pixels, was used to capture the evolution of the shock reflection configuration. Table 1 shows the

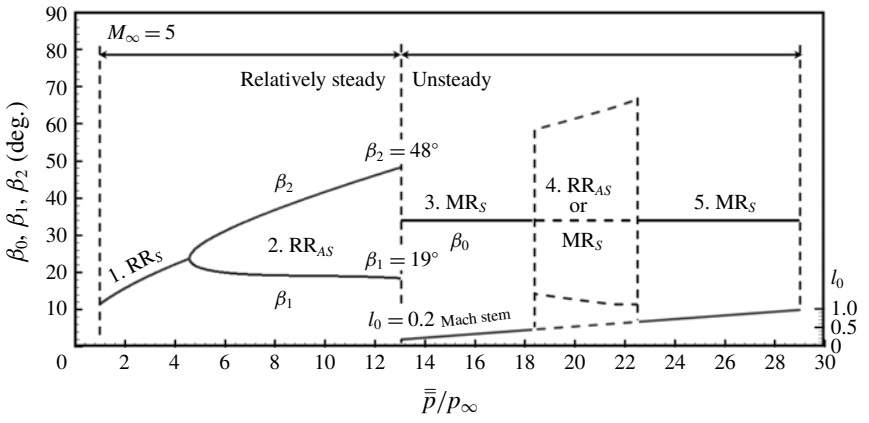

FIGURE 14. Diagram illustrating the relation between $\bar{\bar{p}}$ and shock reflection configurations that fulfill the minimum entropy production.

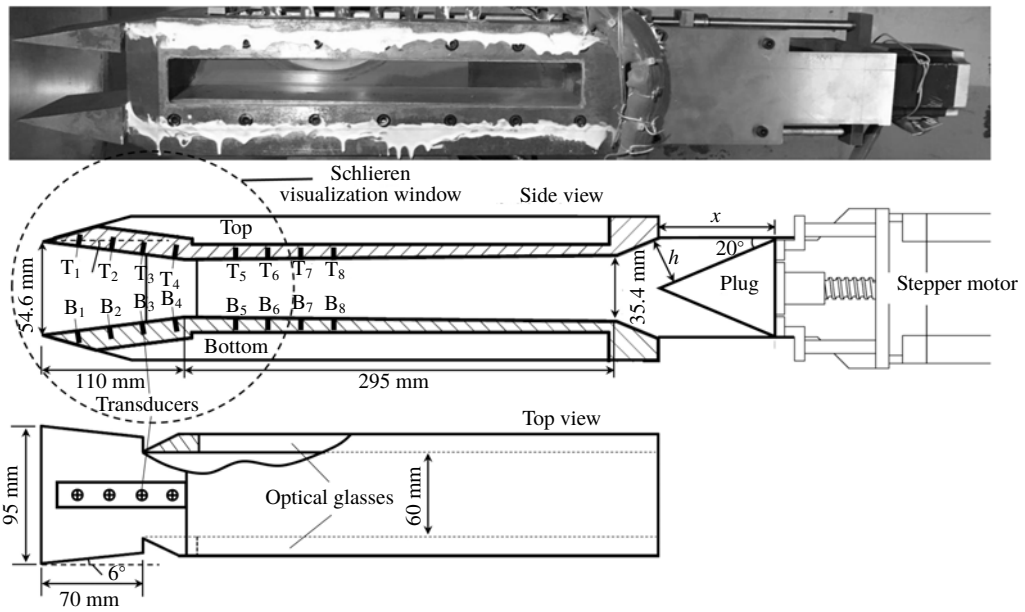

FIGURE 15. Schematic of the test model and downstream throttling device (Wang *et al.* 2017; Xue *et al.* 2018).

test conditions. A non-dimensional variable Δ is defined to measure the downstream throttling:

$$\left.\begin{aligned} \Delta &= \left(1 - \frac{A_{tx}}{A_0}\right) \times 100\,\%, \\ A_{tx} &= 2bx \sin 20°, \end{aligned}\right\} \tag{3.1}$$

where A_{tx} denotes the area size that can flow across the outlet effectively, and A_0 is the total area of the outlet.

Nominal Mach number	5
Calibrated Mach number	4.93
Total temperature (K)	480
Total pressure (kPa)	637
Run time (s)	>7

TABLE 1. Test conditions.

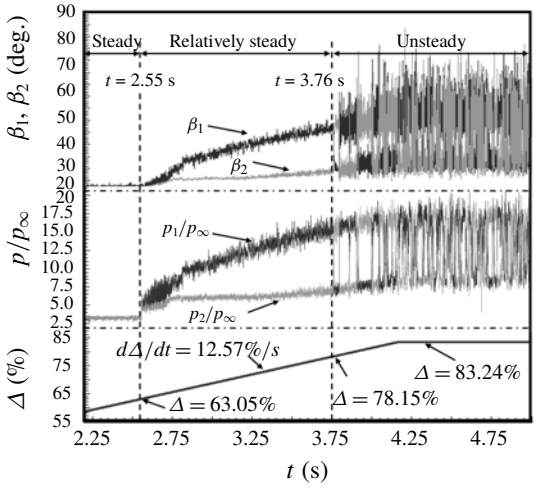

FIGURE 16. Time histories of incident shock angles (β_1, β_2), dynamic wall pressures (p_1, p_2), and downstream throttling degree (Δ).

3.2. *Time history characteristics of incident shock angles and wall pressures*

A quantization method of schlieren images based on a grey-level matrix (see Xue *et al.* 2018) was employed to analyse the dynamic characteristics of the shock configuration, and the time history of shock angles was detected. The experimental results are illustrated in figure 16. In figure 16, β_1 and β_2 are the incident shock angles induced by separation on the top and bottom, respectively; p_1 and p_2 are the dynamic wall pressures obtained by transducers T_1 and B_1 (locations in figure 15), which are the most upstream transducers behind incident shocks on the top and bottom, respectively; and Δ is the downstream throttling degree. Figure 17 shows the standard deviation analysis for illustrating the fluctuation amplitude of p_1, p_2 and $\overline{\overline{p}}$, in which $\overline{\overline{p}}$ is produced by using β_1, β_2, p_1 and p_2 according to the definition of $\overline{\overline{p}}$. Figure 18 shows details of upstream and downstream dynamic pressures as well as $\overline{\overline{p}}$ covering the transition process. Figure 19 shows wall pressure distributions and the accompanying schlieren images during the transition process. As can be indicated, the wall pressures and shock angles were steady with Δ increasing linearly before the appearance of a separation region (figure 16, $t = 2.55$ s, $\Delta = 63.05\,\%$); the shock configuration can be regarded as a relatively steady flow before the RR–MR transition, while it is unsteady after the transition (figure 16, $t = 3.76$ s, $\Delta = 78.15\,\%$). During the RR–MR transition process, downstream pressures turned out to be more stable and symmetrical than upstream ones (figure 19). Although p_1 and p_2 experienced a sharp change in amplitude, $\overline{\overline{p}}$ was more stable (figure 17, $t = 3.76$ s, $\Delta = 78.15\,\%$), which was similar to downstream pressures (figure 18, T_8 and B_8).

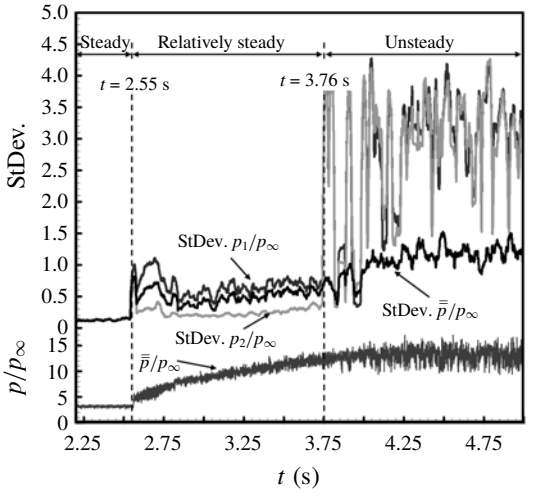

FIGURE 17. Standard deviation analysis of dynamic pressure signals (p_1, p_2 and $\overline{\overline{p}}$) for illustrating the amplitude of pressure fluctuation.

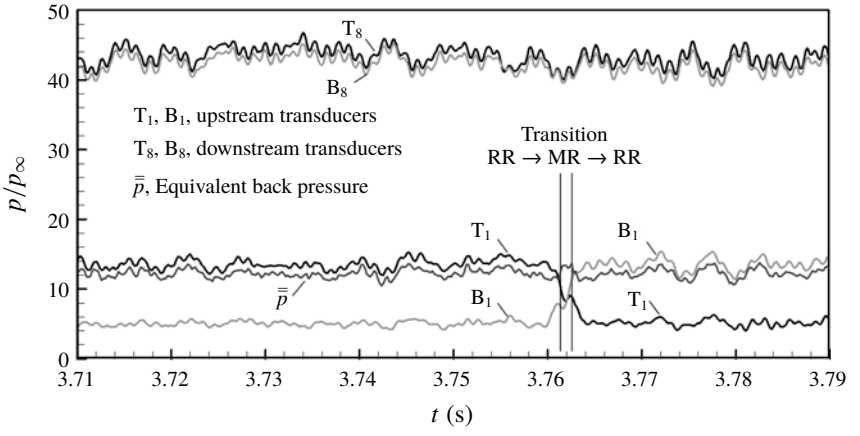

FIGURE 18. Dynamic wall pressures for illustrating shock reflection transition.

The separation-induced shock reflection is mainly generated by downstream pressure disturbance, while the asymmetrical flow configurations as well as transition only exist in the upstream flow field. According to current theory, the estimation of downstream high back-pressure plays an important role in the minimum entropy production principle. However, downstream pressures are hardly connected to upstream flow structures due to the long flow path. Comparing figures 16–19, it is clear that $\overline{\overline{p}}$ is suitable to measure the effect of downstream pressure disturbance. On the one hand, the transition of flow configuration is characterized by the sharp change of upstream wall pressures, while it exerts less influence on downstream wall pressures, which is the same as $\overline{\overline{p}}$ (figures 18 and 19). On the other hand, the original flow disturbance is generated by downstream flow choking measured by Δ, and the positive correlation between Δ and $\overline{\overline{p}}$ is distinct (figures 16 and 17). Therefore, $\overline{\overline{p}}$ changes along with the downstream flow condition and would not be altered by upstream flow

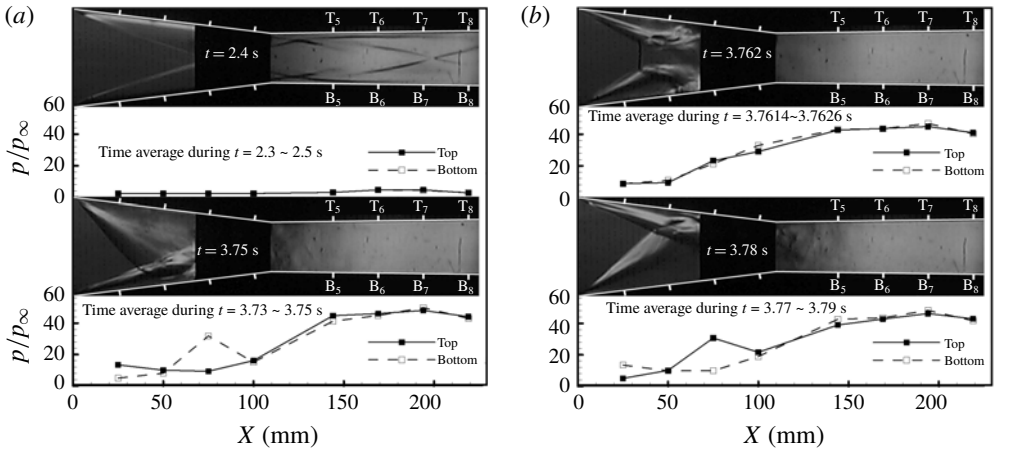

FIGURE 19. Wall-pressure distributions and flow configurations for illustrating shock reflection transition.

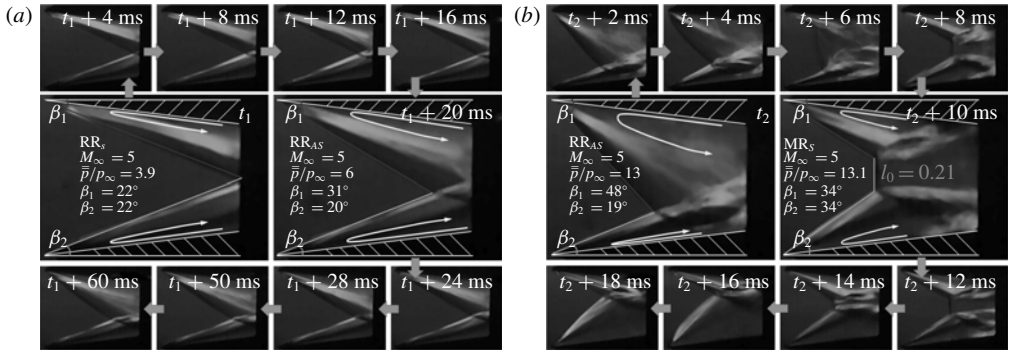

FIGURE 20. The evolution processes of shock configuration transition: (*a*) symmetrical RR to asymmetrical RR, and (*b*) asymmetrical RR to symmetrical MR.

configurations, and it is the same with downstream pressures, which means $\overline{\overline{p}}$ could represent back-pressure. Because $\overline{\overline{p}}$ can be estimated by upstream wall pressures and incident shock angles on the top and bottom, respectively, it can be used as the critical parameter of flow configuration.

3.3. *Evolution processes of shock configuration*

The evolution processes of symmetrical RR to asymmetrical RR transition and asymmetrical RR to symmetrical MR transition are illustrated in figures 20(*a*) and 20(*b*), respectively. As can be seen in figure 20(*a*), the incident shock angle on the top increased smoothly, while it changed indistinctly on the bottom, which demonstrates a gradual transition in symmetrical RR to asymmetrical RR. However, in figure 20(*b*), the process lasted no more than 4 ms from asymmetrical RR to symmetrical MR with a sharp change in $\beta_1 = 48°$ and $\beta_2 = 19°$ to $\beta_1 = \beta_2 = 34°$. Then the configuration turned back to asymmetrical RR immediately, and the subsequent process is asymmetrical RR to symmetrical MR again.

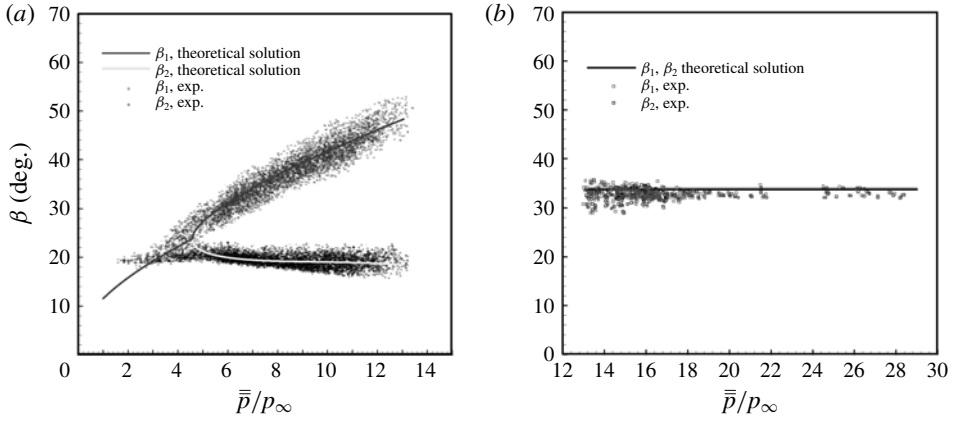

FIGURE 21. Statistical results of incident shock angles detected from schlieren images: (*a*) RR, and (*b*) MR.

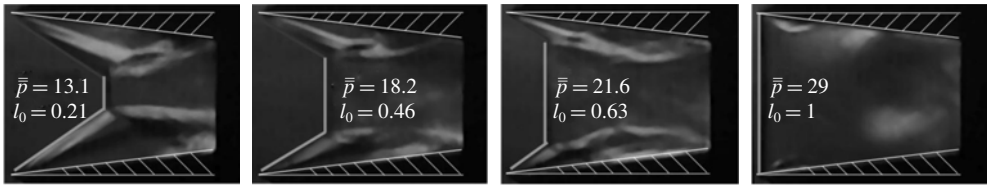

FIGURE 22. Typical MR configurations under the different downstream conditions of $\overline{\overline{p}}$.

The evolution processes demonstrate that it is a relatively steady flow in RR while it is unsteady when RR–MR transition occurs, which is the same as the analysis from dynamic transducer signals. Figure 21 gives the statistical results of incident shock angles including 6000 schlieren images. Figure 22 indicates that the incident shock angles of symmetrical MR under different $\overline{\overline{p}}$ can keep the same degree ($\beta_1 = \beta_2 = 34°$) with an increasing Mach stem (it may be regarded as a normal shock when $\overline{\overline{p}}/p_\infty = 29$ and $l_0 = 1$). The results above demonstrate a good agreement between theory and experiment.

3.4. *Solution path of reflected shock that fulfills the minimum entropy production*

The schlieren images under different $\overline{\overline{p}}$ are selected to illustrate the typical shock configurations, which are shown in figure 23(*a*), and the accompanying reflected shock solutions, *a*–*i*, are depicted via shock polar lines in figure 23(*b*). It is obvious that there is a solution path in the overall RR domain, along which the reflected shock solutions fulfill the minimum entropy production. Based on the comprehensive analysis of theoretical and experimental results, the path is depicted clearly in figure 24, in which the direction means a rising influence of the downstream condition. The path is along a symmetry line at first, then it divides into two opposite paths at the differentiation point, which means the symmetrical configuration fulfills the minimum entropy production with weak enough influence of downstream condition, while it may change to be asymmetrical when the downstream condition increases to a critical level, and the direction chosen by flow is random (as shown in figure 20*a*).

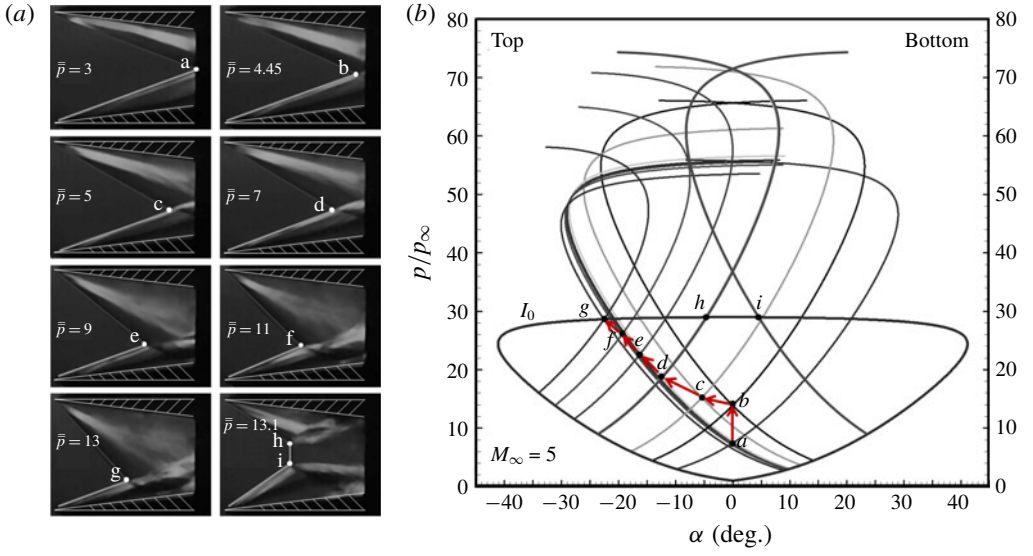

FIGURE 23. (Colour online) Typical (*a*) shock configurations and (*b*) reflected shock solutions under different downstream conditions.

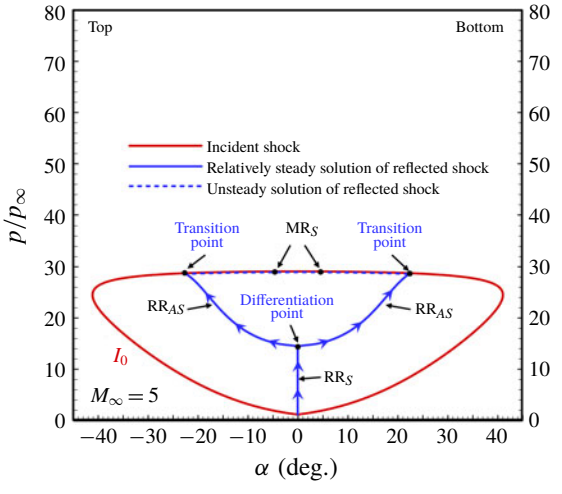

FIGURE 24. (Colour online) The reflected shock solution path that fulfills the minimum entropy production.

When the two divided paths reach the strong polar line of the incident shock at the transition points, the configuration will transform from RR to MR (as shown in figure 20*b*). In fact, when the downstream condition approaches the transition point in the experiment, the RR–MR transition and MR–RR transition will occur repeatedly. The most plausible explanation is that the pressures of the solutions along the dashed path line are too close, and the solutions during the transition process reside on the dashed path line, which means a small downstream pressure disturbance may cause a sharp change in shock structure. Hence, it is confirmed that the solutions on the solid path lines can be regarded as relatively steady, while the solutions on the dashed path

lines are unsteady. Note that the path is produced by the flow itself, which means the flow chooses a way to ensure the solutions fulfill the minimum entropy production under different downstream conditions. Therefore, the solution path can be used to determine the steadiest shock reflection, according to various condition requirements.

4. Conclusions

In the current study, the shock reflection configurations induced by separation are studied theoretically and experimentally. A symmetrical test model with two ramps of 7° is tested in a free-stream flow of Mach number 5, and a downstream throttling device is used to generate the separation region on ramps. The minimum entropy production principle is employed to analyse the shock configurations as well as RR–MR transition. In addition, a variable, represented as $\overline{\overline{p}}$, is proposed to measure the influence of downstream pressure disturbance, based on which the following conclusions are obtained.

The relation among upstream and downstream conditions and shock configurations as well as total entropy production is established by an analytical model. Moreover, separation-induced incident shock angles may be determined by solutions that fulfill the minimum entropy production, and the criterion of RR–MR transition is successfully predicted, which indicate a good agreement with experimental results.

On the other hand, there is a solution path residing in the overall RR domain and the strong incident shock polar line, along which the reflected shock solutions fulfill the minimum entropy production. Furthermore, the shock configuration is relatively steady before the path reaches the strong incident shock polar line, while it is unsteady after that. Therefore, the solution path is very helpful to determine incident shock angles that may induce the steadiest shock configurations in separation-induced flows.

Acknowledgements

This work was supported by the National Natural Science Foundation of China (51776096 and 51476076), and a project funded by the Priority Academic Program Development of Jiangsu Higher Education Institutions (PAPD 016001). This support is gratefully acknowledged.

REFERENCES

AZEVEDO, D. J. & LIU, C. S. 1993 Engineering approach to the prediction of shock patterns in bounded high-speed flows. *AIAA J.* **31**, 83–90.

BAI, C. Y. & WU, Z. N. 2017 Size and shape of shock waves and slip line for Mach reflection in steady flow. *J. Fluid Mech.* **818**, 116–140.

BEN-DOR, G. 1991 *Shock Wave Reflection Phenomena*. Springer.

CHAPMAN, D. R., KUEHN, D. M. & LARSON, H. K. 1958 Investigation of separated flows in supersonic and subsonic streams with emphasis on the effect of transition. *NACA Tech. Rep.* 1356.

CHPOUN, A., PASSEREL, D., LI, H. & BEN-DOR, G. 1995 Reconsideration of oblique shock wave reflections in steady flows. Part 1. Experimental investigation. *J. Fluid Mech.* **301**, 19–35.

CROCCO, L. 1958 One-dimensional treatment of steady gas dynamics. In *Fundamentals of Gas Dynamics* (ed. H. W. Emmons), pp. 110–130. Princeton University Press.

DÉLERY, J. & MARVIN, J. G. 1986 Shock-wave boundary layer interactions. *Tech. Rep.* 280. AGARD.

GAO, B. & WU, Z. N. 2010 A study of the flow structure for Mach reflection in steady supersonic flow. *J. Fluid Mech.* **656**, 29–50.

GLANSDORFF, P. & PRIGOGINE, A. 1971 *Thermodynamic Theory of Structure Stability and Fluctuations*. Wiley.

HORNUNG, H. G., OERTEL, H. & SANDEMAN, R. J. 1979 Transition to Mach reflection of shockwaves in steady and pseudo-steady flow with and without relaxation. *J. Fluid Mech.* **90**, 541–547.

HORNUNG, H. G. & ROBINSON, M. L. 1982 Transition from regular to Mach reflection of shock waves. Part 2. The steady-flow criterion. *J. Fluid Mech.* **123**, 155–164.

HU, Z. M., MYONG, R. S., KIM, M. S. & CHO, T. H. 2009 Downstream flow condition effects on the RR→MR transition of asymmetric shock waves in steady flows. *J. Fluid Mech.* **620**, 43–62.

IVANOV, M. S. I., BEN-DOR, G., ELPERIN, E., KUDRYAVTES, A. N. & KHOTYANOVSKY, D. V. 2002 The reflection of asymmetric shock waves in steady flows: a numerical investigation. *J. Fluid Mech.* **469**, 71–87.

KAWAMURA, R. & SATTO, H. 1956 Reflection of shock waves – 1. Pseudo-stationary case. *J. Phys. Soc. Japan.* **11**, 584–592.

LI, H. & BEN-DOR, G. 1996*a* Application of the principle of minimum entropy production to shock wave reflection. Part I. Steady flow. *J. Appl. Phys.* **80**, 2027–2037.

LI, H. & BEN-DOR, G. 1996*b* Application of the principle of minimum entropy production to shock wave reflection. Part II. Unsteady flow. *J. Appl. Phys.* **80**, 2038–2048.

LI, H., CHPOUN, A. & BEN-DOR, G. 1999 Analytical and experimental investigations of the reflection of asymmetric shock waves in steady flows. *J. Fluid Mech.* **390**, 25–43.

MACH, E. 1878 Uber den verlauf von funkenwellen in der ebeneund im raume. *Sitzugsbr. Akad. Wiss. Wien.* **78**, 819–838.

MATSUO, K., MIYAZATO, Y. & KIM, H. D. 1999 Shock train and pseudo-shock phenomena in internal gas flows. *Prog. Aeronaut. Sci.* **35**, 33–100.

VON NEUMANN, J. 1943 Oblique reflection of shocks. *Tech. Rep.* 12. Navy Department, Bureau of Ordnance, Washington DC.

VON NEUMANN, J. 1945 Refraction, intersection and reflection of shock waves. *Tech. Rep.* 203. Navy Department, Bureau of Ordnance, Washington DC.

TAO, Y., FAN, X. Q. & ZHAO, Y. L. 2014 Viscous effects of shock refection hysteresis in steady supersonic flows. *J. Fluid Mech.* **759**, 134–148.

TAO, Y., LIU, W. D., FAN, X. Q., XIONG, B., YU, J. F. & SUN, M. B. 2017 A study of the asymmetric shock reflection configurations in steady flows. *J. Fluid Mech.* **825**, 1–15.

WANG, C. P., XUE, L. S. & TIAN, X. A. 2017 Experimental characteristics of oblique shock train upstream propagation. *Chin. J. Aeronautics.* **30**, 663–676.

WANG, Z. G., ZHAO, Y. L., ZHAO, Y. X. & FAN, X. Q. 2015 Prediction of massive separation of unstarted inlet via free-interaction theory. *AIAA J.* **53**, 1103–1111.

XUE, L. S., WANG, C. P. & CHENG, K. M. 2018 Dynamic characteristics of separation shock in an unstarted hypersonic inlet flow. *AIAA J.* **56**, 2484–2490.